Multiple Relaxation Time Lattice Boltzmann Models for Multigrid Phase-Field Segmentation of Tumors in 3D Ultrasound Images[*]

Khac L. Nguyen[†], Mohamed M. Tekitek[†], Philippe Delachartre[‡], and Michel Berthier[†]

Abstract. We address the problem of tumor segmentation in 3D ultrasound images. Although many studies have examined this subject, there is still a need to improve segmentation algorithms so as to obtain the best estimation of tumor volumes. In this paper we propose a new approach based on a variational formulation and a multigrid implementation of a multiple relaxation time lattice Boltzmann scheme. The data attachment term, resp., the regularization term, of the energy to be minimized is given by a log-likelihood, resp., the Allen–Cahn reaction diffusion equation. We investigate the stability and accuracy of the proposed scheme with D3Q7 and D3Q19 lattices. Specifically, we show how to choose the relaxation parameters to obtain a fourth-order exact scheme which is shown to be much more relevant than a single relaxation time Bhatnagar–Gross–Krook scheme. Experiments conducted on images with ground truth given by a dermatologist show that the proposed algorithm significantly increases the Dice index (by 10%) and the sensitivity (by 25%) compared with a level set algorithm and is consequently a good alternative to investigate the problem of volume underestimation.

Key words. lattice Boltzmann method, multiple relaxation time, Bhatnagar–Gross–Krook, phase-field method, nonparametric estimation, multigrid, 3D ultrasound images, tumor segmentation

AMS subject classifications. 35Q68, 35Q20, 65C20, 68U10, 68U20

DOI. 10.1137/18M123462X

1. Introduction. This paper addresses the problem of tumor segmentation in 3D ultrasound images. Practically speaking, there are two main difficulties that need to be managed. The first one stems from the intrinsic characteristics of the images, namely, their size (about $300 \times 299 \times 832$ voxels), the fact that the contrast is low, and the presence of speckle noise. The second one comes from the nature of the object to be segmented and the precision required to estimate the volume. Many contributions on this subject emphasize approaches based on graph cut [25] and level set methods [5], [37]. In particular, the latter are well adapted to handle the variability of tumor shapes and speckle patterns. They also provide time-efficient algorithms. However, level set segmentations suffer from one major defect for concrete medical applications. It appears that they tend to underestimate the volume of tumors and that they lack accuracy regarding the detection of the tumor boundary. One of the main objectives of this study was to discuss a new model, from both theoretical and numerical viewpoints, that improves the performance of the segmentation in terms of the Dice index, sensitivity,

[†]MIA, University of La Rochelle, La Rochelle, France (khac.nguyen1@univ-lr.fr, mohamed.tekitek@univ-lr.fr, michel.berthier@univ-lr.fr).
[‡]CREATIS, INSA, Lyon, France (philippe.delachartre@creatis.insa-lyon.fr).

and mean average distance (MAD). This model is based on a variational formulation whose energy is given by a data attachment term and a regularization term. Following [37], the data attachment term is chosen to maximize the log-likelihood distance between intensity distributions inside and outside the region to be segmented. Note that we use a nonparametric estimation based on Parzen estimates [32]. This choice is motivated by arguments involving the specific characteristics of high-frequency images of the skin. It is shown in [37] and [36] that the region surrounding a skin tumor is composed of several tissues of different types that create heterogeneity in the medium. This phenomenon makes use of classical parametric distributions, such as Rayleigh, Rice, Nakagami, or K, inadequate [12]. The main difference from the model studied in [37] is the choice of the regularization part of the energy. The regularization term that we propose aims at creating a smooth diffuse interface of a given size ε that can be thought of as a fuzzification of the boundary sought. A natural choice is the Cahn–Hilliard energy that Γ-converges, when ε tends to 0, to the area of the boundary [4]. The L^2 gradient flow of the Cahn–Hilliard energy is the Allen–Cahn reaction diffusion equation [1], which is known to be a relevant model to describe phase transitions in various physical or chemical applications [20], [17]. Despite its popularity and efficiency in multiphase fluid dynamics, the Allen–Cahn equation is still little used in applications regarding image processing. The reader may refer, for instance, to [28], [18], and [44] for examples of segmentation algorithms based on this equation or to [2] for examples of inpainting models based on the Cahn–Hilliard energy. The experiments discussed in this paper show that the flexibility introduced by the diffuse interface makes it possible to gain accuracy in the detection of the boundary. A significant part of this work is dedicated to the numerical implementation of the gradient flow of the variational formulation mentioned above. We investigate the performances of various lattice Boltzmann schemes [43]. Lattice Boltzmann models (LBMs) are widely used to simulate solutions of physical phenomena, e.g., fluid dynamics, because of their easy parallel implementation; see, for instance, [33]. As applications to image processing, let us mention the contributions of [40], [42] for level set implementations and [9], [23] for denoising and contour detection. One has to note that the use of LBMs in image processing can be problematic. These models are based on time and velocity discretizations of the Boltzmann equation on lattices. The consistency of the discretizations and the stability of the schemes are based on the conservation of several moments which, although they are significant in physical problems, appear to have no real meaning in image processing. This explains why the design of LBM schemes in image processing is still an open question, especially with statistical estimations. The major contribution of this work is the study of the efficiency of multiple relaxation time (MRT) LBM schemes using D3Q7 and D3Q19 lattices [13], [14]. We show in particular how to choose the relaxation parameters to obtain fourth-order exact schemes, the stability of which is numerically established using Von Neumann analysis. These schemes, which are shown to be much more relevant than single relaxation time Bhatnagar–Gross–Krook (BGK) schemes [3], [8], [35] are good examples of the capability of the MRT method to gain accuracy and stability, even in a nonphysical context. Concerning applications, we have conducted experiments on synthetic images as well as on images from a clinical data set. The latter were acquired at the Melanoma Skin Cancer Clinic, Hamilton Hill, Australia. They measure $300 \times 299 \times 832$ voxels, the last number corresponding to depth, with a lateral, resp., depth, resolution of 50, resp., 25 μm. They were chosen to be representative of the diversity

of clinical cases and were manually segmented by a dermatologist. For each one of the 3D images, 150 ground truth contours were drawn in the (x, z)-planes (z is the vertical axis) so as to obtain a 3D volume by interpolation. Comparisons with the level set approach, ADLL, of [37] show that the proposed algorithm significally increases the Dice index (by 10%) and sensitivity (by 25%). It is consequently a good alternative approach to the problem of volume underestimation. The main contributions of this work can be summarized as follows.

– We designed a MRT LBM scheme of a multigrid variational formulation that combines statistical estimations and a phase-field model. To the best of our knowledge, this is the first time that such a scheme has been proposed for image segmentation.

– A rigorous analysis of the consistency and stability of the scheme was conducted. It was shown that, even in a nonphysical context, the MRT approach is a good strategy to obtain relevant performances and leads to schemes that perform much better than BGK schemes.

– Comparisons with a level set–based algorithm on images of a clinical data set show that the proposed algorithm is a good solution to investigate the problem of tumor volume underestimation. Moreover, this algorithm is easy to implement with readily reproducible simulations.

This paper is organized as follows. Section 2 is devoted to the mathematical description of the MRT LBM scheme for phase-field segmentation. The analysis of the consistency and the stability of this scheme is detailed in section 3. In section 4, we propose experiments on synthetic and clinical images and make comparisons with other approaches. We then draw conclusions regarding the work presented.

2. MRT LBM scheme for phase-field segmentation. In this section we describe the lattice Boltzmann schemes based on the variational formulation involving the Cahn–Hilliard energy. The gradient flow corresponding to this variational formulation is a nonlinear diffusion equation [6], [7], [41] whose solution evolves in time to minimize the given energy.

2.1. The variational formulation. The energy we consider is given by

$$(2.1) \qquad E_\epsilon(u) = -LL(u) + \frac{\mu}{c_W} E_\epsilon^{CH},$$

where μ and c_W are constants (see below). The data attachment term, $-LL(u)$, is minus the log-likelihood ratio between intensity distributions inside and outside the region to be segmented [37], and the regularization term E_ϵ^{CH} is the Cahn–Hilliard energy

$$(2.2) \qquad E_\epsilon^{CH}(u) = \int_\Omega \left(\epsilon \frac{|\nabla u|^2}{2} + \frac{1}{\epsilon} W(u) \right) dx.$$

Let us elucidate these two terms. In the last equation W is a double-well potential, typically defined by $W(u) = u^2(1-u)^2/2$. It is well known that the L^2 gradient flow of the Cahn–Hilliard energy is the Allen–Cahn reaction diffusion equation

$$(2.3) \qquad \frac{\partial u}{\partial t} = \left(\epsilon \Delta u - \frac{1}{\epsilon} W'(u) \right).$$

The dynamic of this equation makes the phase-field function u evolve so as to take the two distinct values, 0 and 1, in each of the phases. This process creates a diffuse interface of size ε where u varies smoothly from 0 to 1. The gradient flow of E_ϵ^{CH} is associated with a geometric minimization. It can be shown that the Cahn–Hilliard energy Γ-converges, when ϵ tends to 0, to the area of the transition interface up to the multiplicative constant $c_W = \int_0^1 W(s)ds$, which depends only on W. We refer, for instance, to [19] and [30] for precise statements concerning the Γ-convergence of the minimizers of E_ϵ^{CH} and this geometric interpretation. We consider now that the image to be segmented is divided into two regions. The first one, denoted Ω_A, is the region of interest corresponding for instance to phase 1, and the second one, Ω_B, is the background corresponding to phase 0. It is assumed that the intensity distributions in Ω_A and Ω_B are different. Following [37], the likelihood hypothesis H_1, "the distributions of intensities $I(x)$ in the two regions Ω_A and Ω_B are i.i.d. random variables with different distributions P_A and P_B," is compared to the null hypothesis H_0, "all intensities in Ω_A and Ω_B are i.i.d. random variables from a single distribution $P_{\Omega_A \cup \Omega_B}$." The data attachment term of energy (2.1) is minus the log-likelihood ratio of the two hypothesis, this latter being given by

$$(2.4) \qquad LL = \log\left(\frac{\prod_{x\in\Omega_A} P_A(I(x)) \prod_{x\in\Omega_B} P_B(I(x))}{\prod_{x\in\Omega_A\cup\Omega_B} P_{\Omega_A\cup\Omega_B}(I(x))} \right).$$

We write

$$(2.5) \qquad LL = \sum_{x\in\Omega_A} \log P_A(I(x)) + \sum_{x\in\Omega_B} \log P_B(I(x)) + c,$$

where c is a constant that does not enter into consideration in the minimizing process. In the following, the distributions P_A and P_B are estimated using nonparametric Parzen estimates denoted $\hat{P}_A$ and $\hat{P}_B$. According to the asymptotic equipartition theorem [11], we can replace $(1/|\Omega_A|)\sum_{x\in\Omega_A} \log P_A(I(x))$ with the entropy $\sum_I P_A(I)\log P_A(I)$ (and the same for P_B, $\hat{P}_A$ and $\hat{P}_B$). A simple computation shows that

$$(2.6) \qquad \sum_I \hat{P}_A(I)\log \hat{P}_A(I) = \frac{1}{|\Omega_A|}\sum_{x\in\Omega_A} \log \hat{P}_A(I(x))$$

$$(2.7) \qquad = Div_{KL}(\hat{P}_A\|P_A) + \sum_I P_A(I)\log P_A(I),$$

where Div_{KL} denotes the Kullback–Leibler divergence. Consequently, we may consider that the log-likelihood ratio LL involved in the data attachment term can be written as

$$(2.8) \qquad LL = (S_A + S_B)$$

with

$$(2.9) \qquad S_A = |\Omega_A|\sum_I \hat{P}_A(I)\log \hat{P}_A(I), \quad S_B = |\Omega_B|\sum_I \hat{P}_B(I)\log \hat{P}_B(I),$$

where $|\Omega_A| = \int_{\Omega_A} dx$, $|\Omega_B| = \int_{\Omega_B} dx$ and

$$\text{(2.10)} \qquad \hat{P}_A(I) = \frac{\int u^2 K_\sigma(I(x) - I) dx}{\int u^2 dx},$$

$$\text{(2.11)} \qquad \hat{P}_B(I) = \frac{\int (u - 1)^2 K_\sigma(I(x) - I) dx}{\int (u - 1)^2 dx},$$

are Parzen estimates [24], [32], for the distributions P_A and P_B involving the phase-field function u. In the last equations, K_σ denotes a Gaussian kernel with standard deviation σ. The proof of the following proposition (2.1) is very similar to [37, Appendix A]. As in [37], we assume that $K_\sigma(I(x) - I) \approx \delta(I(x) - I)$, where δ denotes the Dirac distribution. This approximation can be justified by the discrete nature of the data: The values of the Gaussian density are negligible outside the considered voxel if σ is small. We also assume that $\int_{\Omega_A} dx \approx \int_\Omega u^2 dx$ because the profile function minimizing the Cahn–Hilliard energy is of the form $s \longmapsto \frac{1}{2} - \frac{1}{2} \tanh(\frac{s}{2\varepsilon})$ [10], [39]. These approximations are more and more valid as the number of iterations increases. We have the following result.

Proposition 2.1. *Assuming the above approximations, the gradient flow of energy* (2.1) *is given by*

$$\text{(2.12)} \qquad \frac{\partial u}{\partial t} = 2u \log \hat{P}_A(I(x)) + 2(u - 1) \log \hat{P}_B(I(x)) + \frac{\mu}{c_W} \left(\varepsilon \Delta u - \frac{1}{\varepsilon} W'(u) \right).$$

Proof. We compute the functional derivative $\delta S_A / \delta u$

$$\text{(2.13)} \qquad \frac{\delta S_A}{\delta u} = \frac{\delta |\Omega_A|}{\delta u} \sum_I \hat{P}_A(I) \log \hat{P}_A(I)$$

$$\text{(2.14)} \qquad + |\Omega_A| \sum_I \frac{\delta \hat{P}_A(I)}{\delta u} \log \hat{P}_A(I) + |\Omega_A| \sum_I \frac{\delta \hat{P}_A(I)}{\delta u}.$$

Since $|\Omega_A| = \int_{\Omega_A} dx \simeq \int_\Omega u^2 dx$, we have

$$\text{(2.15)} \qquad |\Omega_A| \hat{P}_A(I) = \int u^2 \delta(I(x) - I) dx,$$

$$\text{(2.16)} \qquad \frac{\delta |\Omega_A|}{\delta u} \hat{P}_A(I) + |\Omega_A| \frac{\delta \hat{P}_A(I)}{\delta u} = 2u \delta(I(x) - I),$$

$$\text{(2.17)} \qquad |\Omega_A| \frac{\delta \hat{P}_A(I)}{\delta u} = 2u[\delta(I(x) - I) - \hat{P}_A(I)].$$

Consequently, we obtain

$$\text{(2.18)} \qquad \frac{\delta S_A}{\delta u} = 2u \sum_I \hat{P}_A(I) \log \hat{P}_A(I) + \sum_I 2u[\delta(I(x) - I) - \hat{P}_A(I)] \log \hat{P}_A(I)$$

$$\text{(2.19)} \qquad + \sum_I 2u[\delta(I(x) - I) - \hat{P}_A(I)]$$

and

$$(2.20) \qquad \frac{\delta S_A}{\delta u} = 2u \sum_I \delta(I(x) - I) \log \hat{P}_A(I) + 2u \sum_I \delta(I(x) - I) - 2u \sum_I \hat{P}_A(I).$$

We also have

$$(2.21) \qquad \sum_I \delta(I(x) - I) \log \hat{P}_A(I) \simeq \delta * \log \hat{P}_A(I(x)) = \log \hat{P}_A(I(x)),$$

$$(2.22) \qquad \sum_I \delta(I(x) - I) \simeq \delta * 1 = 1,$$

$$(2.23) \qquad \sum_I \hat{P}_A(I) = 1.$$

This means that

$$(2.24) \qquad \frac{\delta S_A}{\delta u} = -2u \log \hat{P}_A(I(x)).$$

We obtain in the same way

$$(2.25) \qquad \frac{\delta S_B}{\delta u} = -2(u - 1) \log \hat{P}_B(I(x)). \qquad \blacksquare$$

Flow (2.12) can be written as a diffusion equation with a source term

$$(2.26) \qquad \frac{\partial u}{\partial t} = \nabla \cdot (\mathcal{K} \nabla u) + F,$$

where the diffusion coefficient $\mathcal{K}$ is given by

$$(2.27) \qquad \mathcal{K} = \frac{\varepsilon \mu}{c_W},$$

and the source term F reads

$$(2.28) \qquad F = 2u \log \hat{P}_A(I(x)) + 2(u - 1) \log \hat{P}_B(I(x)) - \frac{\mu}{c_W} \frac{1}{\varepsilon} W'(u).$$

The dynamic of gradient flow (2.12) makes the energy E_ϵ decrease to a local minimum that may depends on the chosen initial condition since the underlying optimization problem is nonconvex. At the same time, the L^2 energy $\|u\|_2$ of the solution of the nonlinear diffusion equation may increase in time if the initial condition is located inside the tumor. Figure 1 shows results for the synthetic image shown in Figure 4. In this example, the local minimum is reached after about 70 iterations.
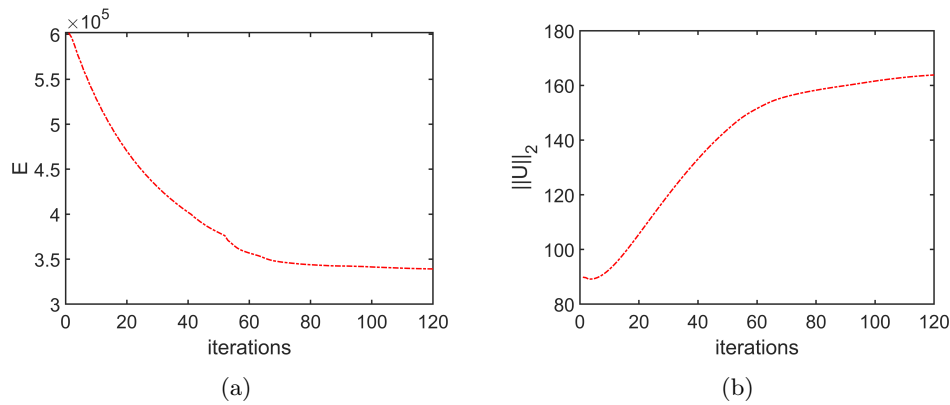
Figure 1. (a) *Energy E_ϵ as time evolves.* (b) *L^2 energy $\|u\|_2$ as time evolves.*

2.2. LBM schemes. LBMs provide very efficient schemes to simulate solutions of physical phenomena, e.g., fluid dynamics. The reader may refer, for instance, to [43] for an introduction and the basic definitions used below. As mentioned before, the major contribution of this work is the design and the rigorous analysis of 3D implementations of the diffusion equation (2.26) using LBM. Lattice Boltzmann equations are a special discretization of the Boltzmann equation. The distribution u depends on space, time, and velocity: $u = u(x, v, t)$. The v-space is discretized by introducing a finite set of $n+1$ weighted velocity directions e_i and associated distribution functions $u_i = u_i(x, t)$, which are governed by the discrete Boltzmann equation. We denote

$$(2.29) \qquad\qquad \mathbf{u} = [u_0, u_1, \ldots, u_n]^T$$

with

$$(2.30) \qquad\qquad u(x, t) = \sum_{i=0}^{n} u_i(x, t)$$

and

$$(2.31) \qquad\qquad \mathbf{F} = [F_0, F_1, \ldots, F_n]^T,$$

where $F_i = t_i F$ with t_i the weight of the lattice in the direction e_i [43]. The discrete Boltzmann equation reads

$$(2.32) \qquad\qquad u_i(x + \tau c_i, t + \tau) = u_i(x, t) + \tau F_i + Q_i$$

for $i = 0, 1, \ldots, n$ and where $c_i = c e_i$ with $c = \delta x / \tau$ the speed of the lattice and δx and τ being the lattice spacing and time step. One usually distinguishes two classes of LBM schemes depending on the choice of the collision operator Q_i, namely, the BGK schemes and the MRT schemes. In the BGK case, also called the single relaxation time (SRT) case, the collision operator is given by

$$(2.33) \qquad\qquad Q_i = \omega(u_i^{eq} - u_i),$$

where ω is the relaxation parameter and

$$(2.34) \qquad \mathbf{u}^{eq} = [u_0^{eq}, u_1^{eq}, \ldots, u_n^{eq}]^T$$

is the equilibrium distribution, typically the Maxwell distribution. For the problem under consideration, it is given by [43]

$$(2.35) \qquad u_i^{eq}(x, t) = t_i u(x, t).$$

The BGK discrete Boltzmann equation is

$$(2.36) \qquad u_i(x + \tau c_i, t + \tau) = (1 - \omega)u_i(x, t) + \omega u_i^{eq}(x, t) + \tau F_i.$$

Since the weight t_i sums to 1, (2.35) expresses the conservation of the moment of order 0. The idea behind MRT schemes is to perform the collision of the particles in the space of momenta so that additional relaxation parameters, which can be adjusted to gain accuracy and stability, can be introduced [13]. The distribution vector $\mathbf{u}$ is mapped by means of a linear transform with matrix $\mathbf{M}$ to the n-dimensional vector space of the first n momenta of the distribution

$$(2.37) \qquad \mathbf{m} = \mathbf{Mu}.$$

The single parameter ω of the BGK approach is replaced by a diagonal matrix $\hat{\mathbf{S}}$ that contains n relaxation parameters. In the same way, the equilibrium distribution u^{eq} is replaced by an n dimensional vector $\mathbf{m}^{eq}$ of equilibrium momenta. The collision term reads

$$(2.38) \qquad \widetilde{\mathbf{m}}(x, t) = (\mathbf{I} - \hat{\mathbf{S}})\mathbf{m}(x, t) + \hat{\mathbf{S}}\mathbf{m}^{eq}(x, t) + \tau \mathbf{F}_{mo}(x, t),$$

where $\mathbf{F}_{mo}$ is the expression of the source term in the space of momenta. After the collision, the streaming process is performed in the initial space,

$$(2.39) \qquad \widetilde{\mathbf{u}}(x, t) = \mathbf{M}^{-1}\widetilde{\mathbf{m}}(x, t),$$
$$(2.40) \qquad u_i(x + \tau c_i, t + \tau) = \widetilde{u}_i(x, t).$$

The MRT collision operator is defined by

$$(2.41) \qquad \mathbf{Qu} = \mathbf{M}^{-1}\hat{\mathbf{S}}\mathbf{M}(\mathbf{u}^{eq} - \mathbf{u}).$$

The numerical experiments we propose in the following are made with D3Q7 and D3Q19 lattices. The choice of these lattices can be justified as follows. The most accurate D3Q27 lattice involves many more computations that do not appear to significantly improve the results of the segmentation. The D3Q15 lattice is known to introduce numerical oscillations due to the checkerboard (parity) invariance problem [14].

2.3. The proposed multigrid scheme. To reduce computation times, a crucial issue for practical use in a clinical context, and to gain accuracy and stability, we propose a multigrid version of flow (2.12). The image is broken down into cells of size a whose coordinates are denoted $\bar{x}$ with $x = a\bar{x}$. We denote also $\bar{u}(\bar{x}, t) = u(x, t)$, $\Omega_{\bar{x}} = \{x \in \bar{x}\}$ and $\hat{P}_{\bar{x}}(I)$ the Parzen estimate of the intensity distribution in the volume $\Omega_{\bar{x}}$. Writing $(\delta E_{\varepsilon}/\delta \bar{u})(\bar{u}) = |\Omega_{\bar{x}}|(\delta E_{\varepsilon}/\delta u)(\bar{u})$, we obtain

$$(2.42) \qquad \frac{\partial \bar{u}}{\partial t} = |\Omega_{\bar{x}}| \left[\frac{\delta S_A}{\delta u}(\bar{u}) + \frac{\delta S_B}{\delta u}(\bar{u}) + \frac{\mu}{c_W} \left(\varepsilon \Delta \bar{u} - \frac{1}{\varepsilon} W'(\bar{u}) \right) \right].$$

The following equation must be satisfied:

$$(2.43) \qquad |\Omega_{\bar{x}}| \frac{\delta S_A}{\delta u}(\bar{u}) = 2\bar{u} \left(\sum_{x \in \bar{x}} \log \hat{P}_A(I(x)) \right).$$

The same holds for S_B. Using the approximation

$$(2.44) \qquad \sum_{x \in \bar{x}} \log \hat{P}_A(I(x)) = \sum_I |\Omega_{\bar{x}}| P_{\bar{x}}(I) \log \hat{P}_A(I),$$

we deduce that

$$(2.45) \qquad \frac{\delta S_A}{\delta u}(\bar{u}) = 2\bar{u} \sum_I \hat{P}_{\bar{x}}(I) \log \hat{P}_A(I)$$

and

$$(2.46) \qquad \frac{\delta S_B}{\delta u}(\bar{u}) = 2(\bar{u} - 1) \sum_I \hat{P}_{\bar{x}}(I) \log \hat{P}_B(I).$$

Finally, up to the multiplicative term $|\Omega_{\bar{x}}|$, the multigrid flow reads

$$(2.47) \quad \frac{\partial \bar{u}}{\partial t} = 2\bar{u} \sum_I \hat{P}_{\bar{x}}(I) \log \hat{P}_A(I) + 2(\bar{u} - 1) \sum_I \hat{P}_{\bar{x}}(I) \log \hat{P}_B(I) + \frac{\mu}{c_W} \left(\frac{\varepsilon}{a^2} \bar{\Delta} \bar{u} - \frac{1}{\varepsilon} W'(\bar{u}) \right),$$

where $\bar{\Delta}$ denotes the Laplacian at scale a. As before, this flow can be written as a diffusion equation with source term

$$(2.48) \qquad F = 2\bar{u} \sum_I \hat{P}_{\bar{x}}(I) \log \hat{P}_A(I) + 2(\bar{u} - 1) \sum_I \hat{P}_{\bar{x}}(I) \log \hat{P}_B(I) - \frac{\mu}{c_W} \frac{1}{\varepsilon} W'(\bar{u})$$

and the diffusion coefficient

$$(2.49) \qquad \mathcal{K} = \frac{\varepsilon \mu}{a^2 c_W}.$$

As mentioned in section 2.2, we consider two MRT LBM implementations of this equation. From now on, we adopt the notations $\Delta x = \delta x$, $\Delta t = |\Omega_{\bar{x}}| \tau$, and $\lambda = \Delta x / \Delta t$. The first

implementation involves a D3Q7 lattice with velocity directions and weights defined by

$$
(2.50) \qquad e_i = \begin{cases} (0,0,0) & i = 0 \\ (\pm 1,0,0), \quad (0,\pm 1,0), \quad (0,0,\pm 1) & i = 1, 2, \ldots, 6 \end{cases}
$$

$$
(2.51) \qquad t_i = \begin{cases} 1/4 & i = 0 \\ 1/8 & i = 1, 2, \ldots, 6. \end{cases}
$$

The transformation matrix $\mathbf{M}$ in (2.37) is

$$
(2.52) \qquad \mathbf{M} = \begin{bmatrix} 1 & 1 & 1 & 1 & 1 & 1 & 1 \\ 0 & \lambda & -\lambda & 0 & 0 & 0 & 0 \\ 0 & 0 & 0 & \lambda & -\lambda & 0 & 0 \\ 0 & 0 & 0 & 0 & 0 & \lambda & -\lambda \\ -6 & 1 & 1 & 1 & 1 & 1 & 1 \\ 0 & 2 & 2 & -1 & -1 & -1 & -1 \\ 0 & 0 & 0 & 1 & 1 & -1 & -1 \end{bmatrix} .
$$

As already noted in the introduction, we can choose the equilibrium momenta so as not to take into account physical properties [29]. In this implementation, these equilibrium momenta are given by

$$
(2.53) \qquad \mathbf{m}^{eq} = (u, 0, 0, 0, \alpha u, 0, 0)^T,
$$

where α is a free parameter. The relaxation matrix we consider is

$$
(2.54) \qquad \hat{\mathbf{S}} = \mathrm{diag}(0, s_1, s_1, s_1, s_2, s_3, s_3),
$$

where s_1, s_2, and s_3 are the relaxation parameters. The vector $\mathbf{F}_{mo}$ is defined by

$$
(2.55) \qquad \mathbf{F}_{mo} = [F, 0, 0, 0, \alpha F, 0, 0]^T.
$$

The second implementation involves a D3Q19 lattice whose velocity directions and weights are given by

$$
(2.56) \qquad e_i = \begin{cases} (0,0,0) & i = 0 \\ (\pm 1,0,0), \quad (0,\pm 1,0), \quad (0,0,\pm 1) & i = 1, 2, \ldots, 6 \\ (\pm 1,\pm 1,0), \quad (\pm 1,0,\pm 1), \quad (0,\pm 1,\pm 1) & i = 7, 8, \ldots, 18 \end{cases}
$$

$$
(2.57) \qquad t_i = \begin{cases} 1/3 & i = 0 \\ 1/18 & i = 1, 2, \ldots, 6 \\ 1/36 & i = 7, 8, \ldots, 18. \end{cases}
$$

The transformation matrix $\mathbf{M}$ in (2.37) is

(2.58)

$$\mathbf{M} = \begin{bmatrix}
1 & 1 & 1 & 1 & 1 & 1 & 1 & 1 & 1 & 1 & 1 & 1 & 1 & 1 & 1 & 1 & 1 & 1 & 1 \\
-30 & -11 & -11 & -11 & -11 & -11 & -11 & 8 & 8 & 8 & 8 & 8 & 8 & 8 & 8 & 8 & 8 & 8 & 8 \\
12 & -4 & -4 & -4 & -4 & -4 & -4 & 1 & 1 & 1 & 1 & 1 & 1 & 1 & 1 & 1 & 1 & 1 & 1 \\
0 & \lambda & -\lambda & 0 & 0 & 0 & 0 & \lambda & -\lambda & \lambda & -\lambda & \lambda & -\lambda & \lambda & -\lambda & 0 & 0 & 0 & 0 \\
0 & -4 & 4 & 0 & 0 & 0 & 0 & 1 & -1 & 1 & -1 & 1 & -1 & 1 & -1 & 0 & 0 & 0 & 0 \\
0 & 0 & 0 & \lambda & -\lambda & 0 & 0 & \lambda & \lambda & -\lambda & -\lambda & 0 & 0 & 0 & 0 & \lambda & -\lambda & \lambda & -\lambda \\
0 & 0 & 0 & -4 & 4 & 0 & 0 & 1 & 1 & -1 & -1 & 0 & 0 & 0 & 0 & 1 & -1 & 1 & -1 \\
0 & 0 & 0 & 0 & 0 & \lambda & -\lambda & 0 & 0 & 0 & 0 & \lambda & \lambda & -\lambda & -\lambda & \lambda & \lambda & -\lambda & -\lambda \\
0 & 0 & 0 & 0 & 0 & -4 & 4 & 0 & 0 & 0 & 0 & 1 & 1 & -1 & -1 & 1 & 1 & -1 & -1 \\
0 & 2 & 2 & -1 & -1 & -1 & -1 & 1 & 1 & 1 & 1 & 1 & 1 & 1 & 1 & -2 & -2 & -2 & -2 \\
0 & -4 & -4 & 2 & 2 & 2 & 2 & 1 & 1 & 1 & 1 & 1 & 1 & 1 & 1 & -2 & -2 & -2 & -2 \\
0 & 0 & 0 & 1 & 1 & -1 & -1 & 1 & 1 & 1 & 1 & -1 & -1 & -1 & -1 & 0 & 0 & 0 & 0 \\
0 & 0 & 0 & -2 & -2 & 2 & 2 & 1 & 1 & 1 & 1 & -1 & -1 & -1 & -1 & 0 & 0 & 0 & 0 \\
0 & 0 & 0 & 0 & 0 & 0 & 0 & 1 & -1 & -1 & 1 & 0 & 0 & 0 & 0 & 0 & 0 & 0 & 0 \\
0 & 0 & 0 & 0 & 0 & 0 & 0 & 0 & 0 & 0 & 0 & 0 & 0 & 0 & 0 & 1 & -1 & -1 & 1 \\
0 & 0 & 0 & 0 & 0 & 0 & 0 & 0 & 0 & 0 & 0 & 1 & -1 & -1 & 1 & 0 & 0 & 0 & 0 \\
0 & 0 & 0 & 0 & 0 & 0 & 0 & 1 & -1 & 1 & -1 & -1 & 1 & -1 & 1 & 0 & 0 & 0 & 0 \\
0 & 0 & 0 & 0 & 0 & 0 & 0 & -1 & -1 & 1 & 1 & 0 & 0 & 0 & 0 & 1 & -1 & 1 & -1 \\
0 & 0 & 0 & 0 & 0 & 0 & 0 & 0 & 0 & 0 & 0 & 1 & 1 & -1 & -1 & -1 & -1 & 1 & 1
\end{bmatrix}.$$

In this implementation, the equilibrium momenta are given by

(2.59) $$\mathbf{m}^{eq} = (u, \alpha u, \beta u, 0, 0, 0, 0, 0, 0, 0, 0, 0, 0, 0, 0, 0, 0, 0, 0)^T,$$

where α and β are free parameters. The relaxation matrix we consider is

(2.60) $$\hat{\mathbf{S}} = \mathrm{diag}(0, s_1, s_2, s_2, s_2, s_2, s_2, s_2, s_2, s_1, s_2, s_1, s_2, s_1, s_1, s_1, s_2, s_2, s_2),$$

where s_1 and s_2 are the relaxation parameters. The vector $\mathbf{F}_{mo}$ is defined by

(2.61) $$\mathbf{F}_{mo} = [F, \alpha F, \beta F, 0, 0, 0, 0, 0, 0, 0, 0, 0, 0, 0, 0, 0, 0, 0, 0]^T.$$

The resulting algorithm is described in (2.1), where we drop the overbar to simplify the notations. Note that we use the so-called strong splitting [21] when adding the source term in the moment space. The main loop of the algorithm stops when the L^2 distance between two successive iterations is less than 0.1% (moment evaluation). Finally, the segmented region of interest is the set where $u \geq 1/2$. In the experiments described below we compare this new implementation with the BGK implementation of [9].

3. Consistency and stability of the LBM MRT multigrid phase-field schemes. We explain in this section how to choose the various parameters of the MRT schemes described above in order to gain accuracy and stability. This is a crucial step that may lead to confusion when comparing LBM implementation strategies. For instance, in [31], the authors cannot find relevant parameters for MRT schemes. As shown in the following and concerning our application, MRT schemes perform much better than BGK schemes when parameters are suitably tuned.

Algorithm 2.1 LBM MRT multigrid phase-field segmentation.

Initialize u
Compute source term F
Compute source lattice vector $\mathbf{F}$
Compute $\mathbf{M}$, $\mathbf{M}^{-1}$, $\hat{\mathbf{S}}$ and $\mathbf{F}_{mo}$
while Tol $> 10^{-3}$ **do**
  Map to moment space: $\mathbf{m}^{(k)} = \mathbf{M}\mathbf{u}^{(k)}$
  Add source term (strange splitting): $\mathbf{m}^{(k)} \leftarrow \mathbf{m}^{(k)} + \Delta t \mathbf{F}_{mo}^{(k)}/2$
  Evaluate moments
  Do collision (moment relaxation): $\mathbf{m}^{(k)} \leftarrow (\mathbf{I} - \hat{\mathbf{S}})\mathbf{m}^{(k)} + \hat{\mathbf{S}}\mathbf{m}^{eq(k)}$
  Add source term (strange splitting): $\mathbf{m}^{(k)} \leftarrow \mathbf{m}^{(k)} + \Delta t \mathbf{F}_{mo}^{(k)}/2$
  Map to initial space: $\mathbf{u}^{(k)} = \mathbf{M}^{-1}\mathbf{m}^{(k)}$
  Compute boundary conditions: anti-bounce back conditions
  Do streaming: $u_i^{(k+1)}(x + c_i\tau, t + \tau) \leftarrow u_i^{(k+1)}(x, t)$
  Update distribution: $u = u_0 + \cdots + u_n$
  Update source term F
  Update source lattice vector $\mathbf{F}_{mo}$
end while
return u

3.1. Consistency. We follow the approach of [16], where the authors explain how to adjust the so-called quartic relaxation parameters in order to enforce fourth-order accuracy for the thermal model and diffusive relaxation modes of the Stokes problem. Recall that the parameters of the D3Q7 MRT scheme are α, s_1, s_2, and s_3 and that those of the D3Q19 MRT scheme are α, β, s_1, and s_2. We drop the overbar to simplify notations.

Proposition 3.1. There exist sets of parameters so that the D3Q7 and D3Q19 MRT diffusion schemes are fourth-order consistent, i.e.,

$$(3.1) \qquad \frac{\partial u}{\partial t} - \nabla \cdot (\mathcal{K}\nabla u) = O(\Delta t^4),$$

and thus free of numerical diffusion.

Proof. We refer to [16] for details and give only the main arguments of the proof. Recall that λ denotes the $\Delta x/\Delta t$ ratio. Using Taylor expansions, one can show that

$$(3.2) \qquad \frac{\partial u}{\partial t} - \nabla \cdot (\mathcal{K}\nabla u) + A\Delta t^2 + B\Delta t^3 = O(\Delta t^4)$$

with

$$(3.3) \qquad \mathcal{K} = \frac{\lambda^2}{21}\Delta t(6 + \alpha)\left(\frac{1}{s_1} - \frac{1}{2}\right)$$

for the D3Q7 scheme and

$$(3.4) \qquad \mathcal{K} = \frac{\lambda^2}{57}\Delta t(30 + \alpha)\left(\frac{1}{s_2} - \frac{1}{2}\right)$$

for the D3Q19 scheme. Choosing the following quartic parameters for the D3Q7 scheme

$$(3.5) \qquad s_2 = \left[\frac{6+\alpha}{1-\alpha} \left(\frac{1}{s_1} - \frac{1}{2} \right) + \frac{3\alpha + 4}{12(\alpha - 1)\left(\frac{1}{s_1} - \frac{1}{2} \right)} + \frac{1}{2} \right]^{-1},$$

$$(3.6) \qquad s_3 = \left[\frac{1}{6\left(\frac{1}{s_1} - \frac{1}{2} \right)} + \frac{1}{2} \right]^{-1},$$

we obtain $A = B = 0$ in (3.2). In the same way as [26], choosing the following quartic parameters for the D3Q19 scheme

$$(3.7) \qquad s_1 = \frac{1}{\frac{1}{\sqrt{3}} + \frac{1}{2}}, \qquad s_2 = \frac{2}{\frac{1}{\sqrt{3}} + 1},$$

we also obtain $A = B = 0$ in (3.2).   ∎

In the experiments described below, we set $s = s_1 = 2/(1/\sqrt{3} + 1)$ for the D3Q7 scheme and $s = s_2 = 2/(1/\sqrt{3} + 1)$, $\beta = 0$ for the D3Q19 scheme. The values of all the other parameters are set by the value of the diffusion coefficient $\mathcal{K}$.

3.2. Stability. We propose numerical experiments in order to demonstrate the stability of the D3Q7 and D3Q19 schemes when dealing with the above choice of quartic parameters. These experiments are based on the classical Von Neumann analysis in the Fourier space (see [27]). The initial condition is given by a plane wave of small amplitude with a wave vector $k = (k_x, \ k_y, \ k_z)$, a uniform density u, and possibly a uniform vector velocity $V = (V_x, V_y, V_z)$. Let

$$(3.8) \qquad f = f^0 + \delta f,$$

where $f^0 = (f_0, \ldots, f_q)$ ($q = 6$ for the D3Q7 scheme and $q = 18$ for the D3Q19 scheme) represents the uniform equilibrium state specified by the uniform and steady density u and the vector velocity $V = (V_x, V_y, V_z)$ and δf is a small perturbation. In our context, there is no convection, and therefore we can choose $V_x = V_y = V_z = 0$. Inserting (3.8) in the the discrete Boltzamnn equation (2.32) with collision operator (2.41) leads to

$$(3.9) \qquad f(x, t + \Delta t) = Gf(x, t),$$

where G is the amplification matrix. Let $p = e^{i\,k_x}$, and let $q = e^{i\,k_y}$ and $r = e^{i\,k_z}$ be the phase factors. The amplification matrix G of the D3Q7 scheme can be written as the product

$$(3.10) \qquad G = P\mathbf{M}^{-1}\Psi\mathbf{M},$$
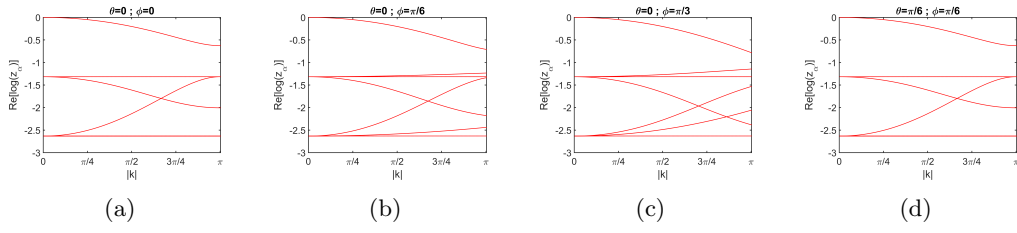
Figure 2. *Logarithmic eigenvalues $Re[\ln(z_\alpha)]$ versus absolute value of wave number $|k|$ for the $D3Q7$ scheme.* (a) *The wave number k has azimuthal angle $\theta = 0$ and polar angle $\phi = 0$;* (b) $\theta = 0$, $\phi = \pi/6$; (c) $\theta = 0$, $\phi = \pi/3$; (d) $\theta = \pi/6$, $\phi = \pi/6$.

where

(3.11) $$P = \mathrm{diag}(1, p, 1/p, q, 1/q, r, 1/r),$$

(3.12) $$\Psi = \begin{bmatrix} 1 & 0 & 0 & 0 & 0 & 0 & 0 \\ 0 & s_1 & 0 & 0 & 0 & 0 & 0 \\ 0 & 0 & s_1 & 0 & 0 & 0 & 0 \\ 0 & 0 & 0 & s_1 & 0 & 0 & 0 \\ 0 & 0 & 0 & 0 & s_2 & 0 & 0 \\ 0 & 0 & 0 & 0 & 0 & s_3 & 0 \\ 0 & 0 & 0 & 0 & 0 & 0 & s_3 \end{bmatrix},$$

and $\mathbf{M}$ is given by (2.52). The stability of the scheme is based on (3.9), which is an eigenvalue problem and therefore requires the determination of the eigenvalues of the amplification matrix G. These eigenvalues are obtained by numerically solving the following dispersion equation [27]

(3.13) $$\det(G - z\ Id) = 0\,,$$

where $z = e^{i\Delta t}$ is the time factor. The scheme becomes unstable when one of the eigenvalues of G is greater than 1 or equivalently when one of the solutions z_j, $j = 1, 2\ldots, 7$, of the dispersion equation (3.13) satisfies $\Re(\ln z_j) \geq 0$ [38]. Simulations illustrated in Figure 2 show that the D3Q7 scheme is effectively stable when considering the quartic parameters chosen. A similar study can be conducted for the D3Q19 scheme. The results are shown in Figure 3.

4. Experiments. First, we propose expriments on two kinds of synthetic images to emphasize the importance of the multigrid aspect of the proposed algorithm. We investigated only the D3Q7 case; similar results can be obtained with the D3Q19 scheme. In terms of stability, we then compared the above-described MRT schemes (with well-chosen quartic parameters) with a BGK, SRT scheme using both synthetic and clinical images. Finally, we describe the results obtained on eight images from a clinical data set with ground truth given by a dermatologist and compare these results with those given by the ADLL level set algorithm of [37]. We make use of the four following classical measurements to evaluate the performance of the segmentation [15], [34]. Let us denote Ω and R the segmented and the reference volumes to be compared.
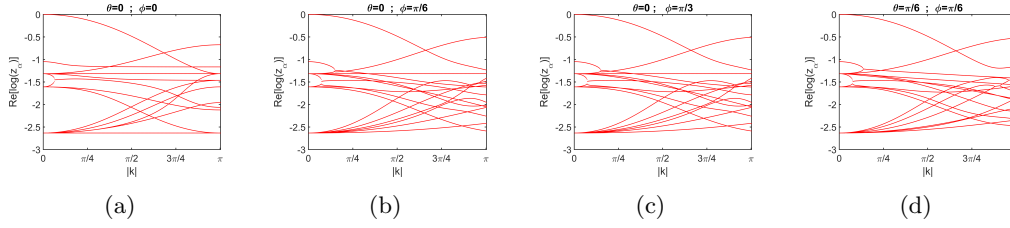
Figure 3. *Logarithmic eigenvalues $Re[\ln(z_\alpha)]$ versus absolute value of wave number $|k|$ for the $D3Q19$ scheme.* (a) *The wave number k has azimuthal angle $\theta = 0$ and polar angle $\phi = 0$;* (b) *$\theta = 0$, $\phi = \pi/6$;* (c) *$\theta = 0$, $\phi = \pi/3$;* (d) *$\theta = \pi/6$, $\phi = \pi/6$.*

 – The sensitivity S is defined by $S(\Omega, R) = |\Omega \cap R|/|R|$.
 – The precision P is defined by $P(\Omega, R) = |\Omega \cap R|/|\Omega|$.
 – The Dice index is given by the harmonic mean of S and P

$$(4.1) \qquad\qquad D(\Omega, R) = \frac{2|\Omega \cap R|}{|\Omega| + |R|} \, .$$

 – The mean absolute distance makes it possible to determine if the boundary of the segmented volume fits well with the boundary of the reference volume. Let us denote $N_{\partial\Omega}$, resp., $N_{\partial R}$, the number of voxels in the boundary $\partial\Omega$, resp., ∂R, of the segmented, resp., reference, volume. The (symetric) $\mathrm{MAD}(\Omega, R)$ is defined by

$$(4.2) \qquad\qquad \mathrm{MAD}(\Omega, R) = \sum_{x \in \partial\Omega} \frac{d(x|R)}{2\mathrm{surf}(\partial\Omega)} + \sum_{x \in \partial R} \frac{d(x|\Omega)}{2\mathrm{surf}(\partial R)} \, .$$

In this definition, $d(x|R) = \min_{x' \in \partial R} \|x' - x\|$ is the distance of the point x to the boundary ∂R, and the same replacing R with Ω. The terms $\mathrm{surf}(\partial R)$ and $\mathrm{surf}(\partial\Omega)$ denote the number of voxels in the boundaries ∂R and $\partial\Omega$. Note that the MAD is measured in μm. In practice, it can be useful to adjust the double-well potential $W(u)$ to improve the segmentation. Let us denote W_θ the potential defined by $W_\theta(u) = \theta W(u)$. A simple computation shows that the diffusion coefficient $\mathcal{K} = \mu\varepsilon/a^2 c_W$ of (2.47) becomes $\mathcal{K} = \mu\varepsilon'/a^2 c_W$ with $\theta\varepsilon' = \varepsilon$ and that the coefficient $\mu/\varepsilon c_W$ of $W'(u)$ becomes $\mu/\varepsilon'\theta c_W$. This means that (2.47) is now considered to involve three parameters, namely, μ, ε, and θ. Choosing μ and $\mathcal{K}$ determines ε and the relaxation parameters of the MRT scheme. In all of the experiments the space step Δx is given by $\Delta x = 1/N$ with $N = \max(N_x, N_y, N_z)$ with N_x, N_y, and N_z the number of pixels in each of the directions of the image. In short, the parameters that have to be tuned for the experiments are μ, $\mathcal{K}$, θ; the time step Δt; and the scale a.

4.1. D3Q7 multigrid phase-field segmentation of synthetic images. The first synthetic image we consider is shown in Figure 4. It measures $256 \times 256 \times 256$ voxels, that is, about 17 million voxels. It is corrupted by a Rayleigh distribution noise. The segmentation is performed at scales $a = 1, 2, 3, 4, 5$. The time step is set as $\Delta t = 0.002$ to ensure stability at the initial scale $a = 1$. We choose $\mathcal{K} = 0.4 \times 10^{-3}$, $\mu = 0.02$, and $\theta = 10/a^2$. The results are presented in Table 1. We can see that the Dice index slightly decreases when

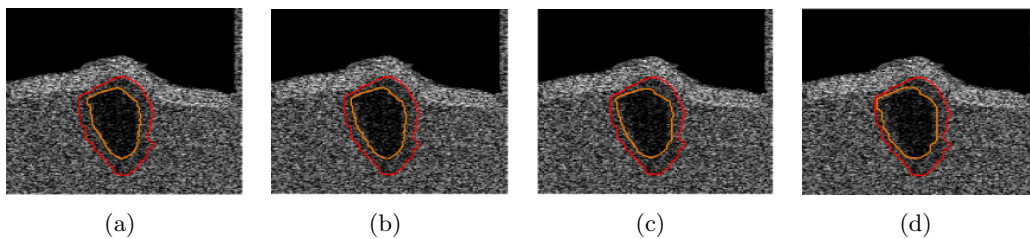(a) (b) (c) (d) (e)
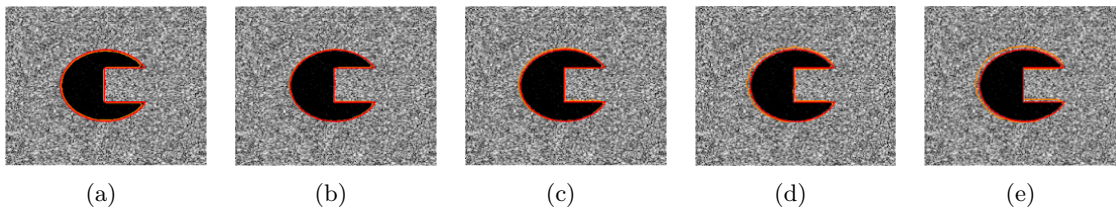
Figure 4. *D3Q7 MRT segmentation results for a simple synthetic image at different scales:* (a) $a = 1$, (b) $a = 2$, (c) $a = 3$, (d) $a = 4$, (e) $d = 5$. *The time step is set as* $\Delta t = 0.002$. *Reference contour in red.*

Table 1
D3Q7 MRT segmentation results for a simple synthetic image at different scales and time step set as $\Delta t = 0.002$.

a	D	S	P	MAD (pixels)	$Times$ (seconds)
1	0.950	0.906	0.999	1.283	33447
2	0.978	0.976	0.980	0.663	1271
3	0.957	0.987	0.929	1.206	173
4	0.931	0.986	0.882	1.893	152
5	0.917	0.986	0.857	2.260	84

(a) (b) (c) (d)

Figure 5. *D3Q7 MRT segmentation results for a synthetic image of a tumor at different scales:* (a) $a = 1$, (b) $a = 2$, (c) $a = 3$, (d) $a = 4$, (e) $d = 5$. *The time step is set as* $\Delta t = 0.002$. *Reference contour in red.*

the scale increases. In contrast, the sensitivity increases. This can be explained by the fact that the flow dynamics are less conservative at higher scales and by the large number of iterations needed to get convergence at the initial scale [22]. Computation times of a simple (nonparallel) implementation show that the large size of the image does not allow reasonable segmentations at scale 1 or 2. Working at scale 3, one obtains a speed-up factor of about 2000. Moreover, at higher scales the step time can be chosen much greater than 0.002. For a second test we consider a synthetic image of a tumor measuring $322 \times 142 \times 172$ voxels corrupted by a Rayleigh distribution noise; see Figure 5. The parameters are given by $\mathcal{K} = 0.2 \times 10^{-3}$, $\mu = 0.001$, $\theta = 10/a^2$, and $\Delta t = 0.002$. The results are presented in Table 2. These results confirm the observations made in the previous case.

We focus now on scales 3 and 4 and increase the time step, which is impossible at scales 1 and 2 without losing stability. We set $\Delta t = 0.03$. The results of the segmentation are shown in Figure 6 and evaluated in Table 3. Increasing the time step makes the flow dynamic less conservative and gives much better results in terms of both segmentation and computation

Table 2

D3Q7 MRT segmentation results for a synthetic image of a tumor at different scales. The time step is set as $\Delta t = 0.002$.

a	D	S	P	MAD (pixels)	Times (seconds)
1	0.595	0.423	1.000	7.020	6095
2	0.623	0.452	1.000	6.614	816
3	0.635	0.465	0.998	6.534	179
4	0.679	0.516	0.995	5.807	79

(a)   (b)
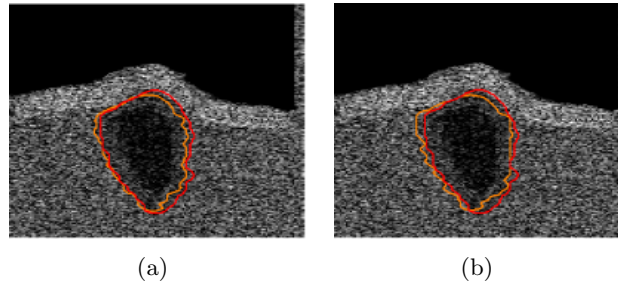
Figure 6. *D3Q7 MRT segmentation results for a synthetic image of a tumor at scales (a) $a = 3$ and (b) $a = 4$. The time step is set as $\Delta t = 0.03$. Reference contour in red.*

Table 3

D3Q7 MRT segmentation results for a synthetic image of a tumor at scales $a = 3$ and $a = 4$. The time step is set as $\Delta t = 0.03$.

a	D	S	P	MAD (pixels)	Times (seconds)
3	0.902	0.854	0.956	1.844	56
4	0.887	0.868	0.908	2.146	21

times. For example, in the case $a = 4$ and compared with the previous time step $\Delta t = 0.002$, the Dice index and MAD are improved by 31% and 63%, respectively, and the computational time is decreased by 73%. These first experiments clearly show the advantages of the multigrid approach: It makes the algorithm more stable, it significantly reduces the computation time, and it improves the results of the segmentation.

4.2. MRT versus BGK segmentation. We concentrate now on comparing the proposed MRT scheme with a classical BGK, SRT scheme using both the D3Q7 and D3Q19 lattices. The aim is to show the benefit of introducing additional relaxation parameters to gain stability. For each scheme, we compute the relative error

$$(4.3) \qquad err = \frac{\|u^{n+1} - u^n\|_2}{\|u^n\|_2} \ ,$$

where $u^n = u(t^n = n\delta t)$. This relative error should decrease in time if the scheme is numerically stable. For the first comparison, we make use of the synthetic image of a tumor introduced before. The parameters are set as follows: $\mathcal{K} = 0.3 \times 10^{-3}$, $\mu = 0.01$, $\theta = 1$, $\Delta t = 0.04$, and $\Delta t = 0.05$. The scale is $a = 4$. The results of the simulations are shown
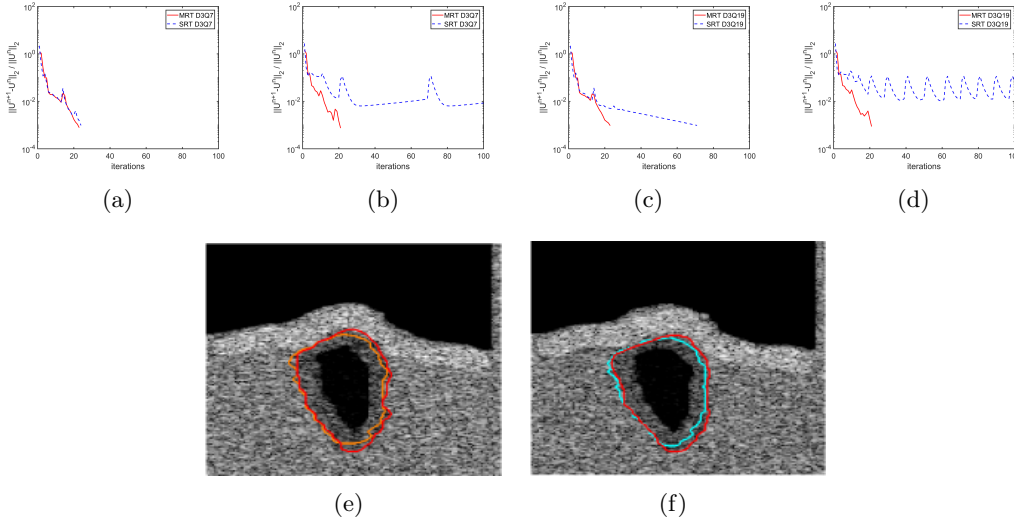
Figure 7. *Stability comparison performed on the synthetic image of a tumor. $D3Q7$ lattice: (a) time step: $\Delta t = 0.04$, (b) time step $\Delta t = 0.05$. $D3Q19$ lattice: (c) time step: $\Delta t = 0.04$, (d) time step $\Delta t = 0.05$. One slice of the MRT LBM phase-field segmentation: (e) $D3Q7$ lattice and time step $\Delta t = 0.05$, (f) $D3Q19$ lattice at the time step $\Delta t = 0.05$. Reference contour in red.*
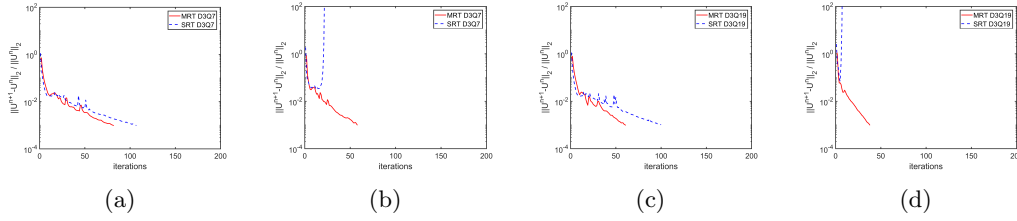
Figure 8. *Stability comparison performed on an image of the clinical data set Figure 10(d). $D3Q7$ lattice: (a) time step $\Delta t = 0.015$, (b) time step $\Delta t = 0.025$. $D3Q19$ lattice: (c) time step $\Delta t = 0.015$, (d) time step $\Delta t = 0.035$.*

in Figure 7. In the D3Q7 case, we can see that the BGK scheme is much more sensitive to increasing the time step Δt and becomes clearly unstable for $\Delta t = 0.05$, whereas the MRT scheme behaves in the same way. The D3Q19 case confirms this observation and shows that the instability of the BGK scheme is not caused by the choice of the lattice. We reach the same conclusion when using the image 10(d) of the clinical data set. The parameters are set as follows: $\mathcal{K} = 0.5 \times 10^{-3}$, $\mu = 0.079$, $\theta = 1$, $\Delta t = 0.015$, and $\Delta t = 0.025$. The scale is $a = 4$. The results of the simulations are shown in Figure 8. In conclusion, it appears that the MRT approach is a good strategy to obtain relevant performance and leads to schemes that behave much better than BGK schemes.

4.3. MRT multigrid phase-field segmentation of clinical images.
We now evaluate the proposed MRT scheme using the eight images of clinical data set 10. Let us recall that these images were chosen to be representative of the diversity of clinical cases and were manually
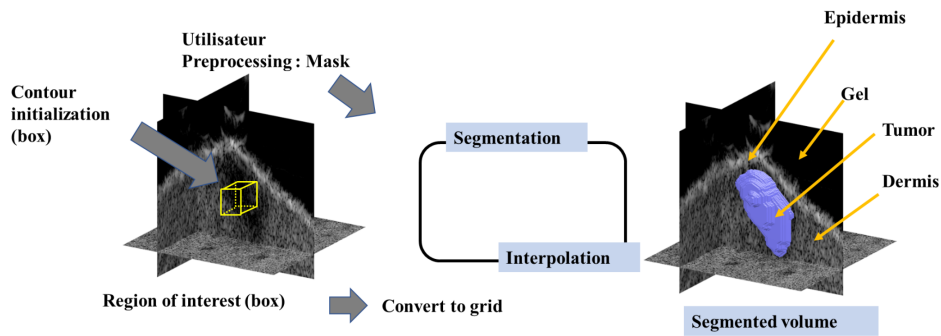
Figure 9. *MRT LBM phase-field segmentation process for clinical images.*
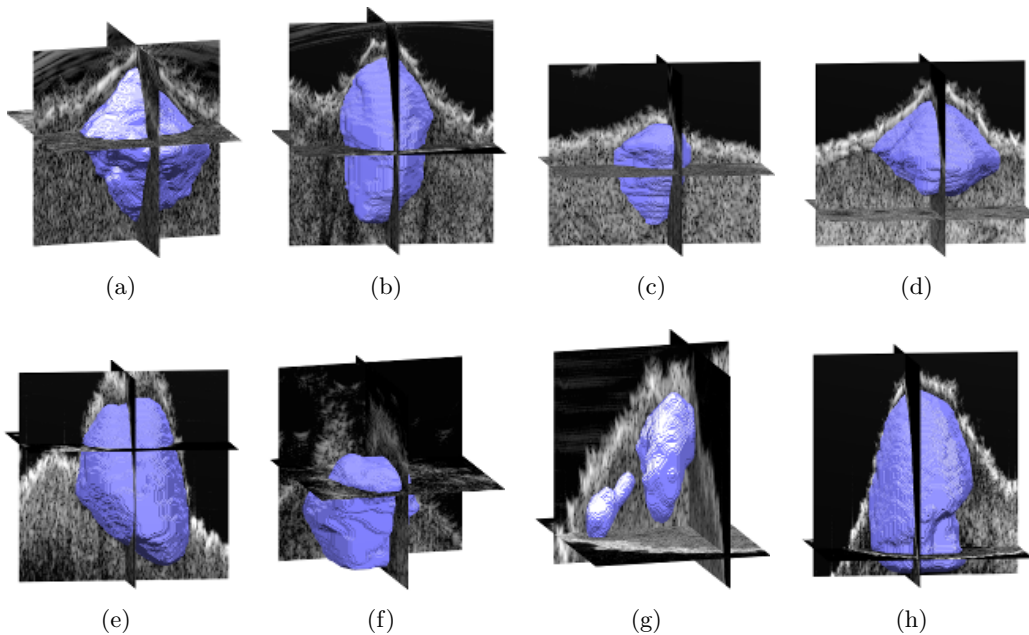

Figure 10. *Images from the clinical data set and results of the LBM MRT D3Q7 segmentation.*

segmented by a dermatologist. For each one of the 3D images, 150 ground truth contours are drawn in the (x, z)-planes (z is the vertical axis) so as to obtain a 3D volume by interpolation. Nearly 50 values of the intensity I are retained, and the gel area (black area above the epidermis) is removed before the tumor segmentation is performed. The entire process in described in Figure 9, and the results of the segmentation with the LBM MRT D3Q7 algorithm are shown in Figure 10. The main objective of this section is to use the ADLL algorithm of [37], based on a level set approach, for comparisons and to show that the new algorithm is relevant for investigating the problem of the underestimation of the segmented volume. Let us specify that the ADLL and the proposed MRT algorithms share the same data attachment term and therefore that the difference between segmentation is only due to the regularization

Table 4
Comparisons between ADDL level set [37], LBM MRT D3Q7, and LBM MRT D3Q19 algorithms.

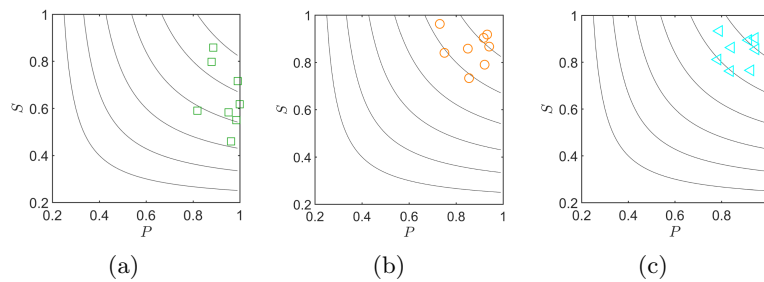| Algorithm	D	S	P	MAD (pixels)
ADLL	0.755 ± 0.086	0.647 ± 0.134	0.934 ± 0.065	344 ± 106
MRT D3Q7	0.857 ± 0.052	0.859 ± 0.073	0.862 ± 0.082	202 ± 78
MRT D3Q19	0.858 ± 0.048	0.849 ± 0.064	0.873 ± 0.068	199 ± 68

Figure 11. *Sensitivity S versus precision P. (a) ADLL level set [37]. (b) LBM MRT D3Q7 lattice. (c) LBM MRT D3Q19 lattice.*

term and the implementation. The performance indicators are given in Table 4. The scale is $a = 4$. The parameters are tuned adaptively so as to maximize the Dice index for each lesion. They are chosen as follows. For the ADLL algorithm, $\mu \in [0.001, 0.01]$, $\Delta t \in [0.8, 2]$, and $T = [2, 10]$. For the MRT D3Q7 algorithm, $\mathcal{K} \in [0.27 \times 10^{-3}, 1 \times 10^{-3}]$, $\mu \in [0.132, 0.113]$, $\Delta t \in [0.01, 0.025]$, and $\theta \in [0.01, 3]$. For the MRT D3Q19 algorithm, $\mathcal{K} \in [0.3 \times 10^{-3}, 2 \times 10^{-3}]$, $\mu \in [0.01, 0.16]$, $\Delta t \in [0.01, 0.04]$, and $\theta \in [0.0056, 1.5]$.

It is not surprising that the ADLL algorithm gives the best precision P. Let us recall that precision measures the fact that the segmented volume is indeed part of the tumor. However, this segmented volume is too small, as it is confirmed by the sensitivity and the MAD. Sensitivity measures the fact that the entire tumor has been segmented and the MAD is the average distance to the boundary of the tumor. Quantitively, the sensitivity of the ADLL algorithm is about 25% lower. As a consequence, the Dice index is also lower, about 14%. This means that the proposed algorithm performs better regarding the ability to segment the entire tumor. Moreover, this algorithm gives a MAD about 42% higher than the ADLL algorithm, which is a very significant improvement of the performance concerning the detection of the boundary of the tumor. A compact presentation of these results is given in the trade-off Figure 11 with the level sets of the Dice index. Slices of segmentations are shown in Figure 12.

The results of the MRT D3Q7 and MRT D3Q19 algorithms are very similar. For obvious reasons due to computation costs, one finally may prefer the MRT D3Q7 implementation.

5. Conclusion. We have described a new algorithm for tumor segmentation in 3D ultrasound images. This algorithm is based on a variational formulation whose regularization term is given by a phase-field model, namely, the Allen–Cahn reaction diffusion equation. An original implementation of the corresponding gradient flow using LMB MRT schemes has been discussed. It has been shown that it is possible to choose the relaxation quartic parameters
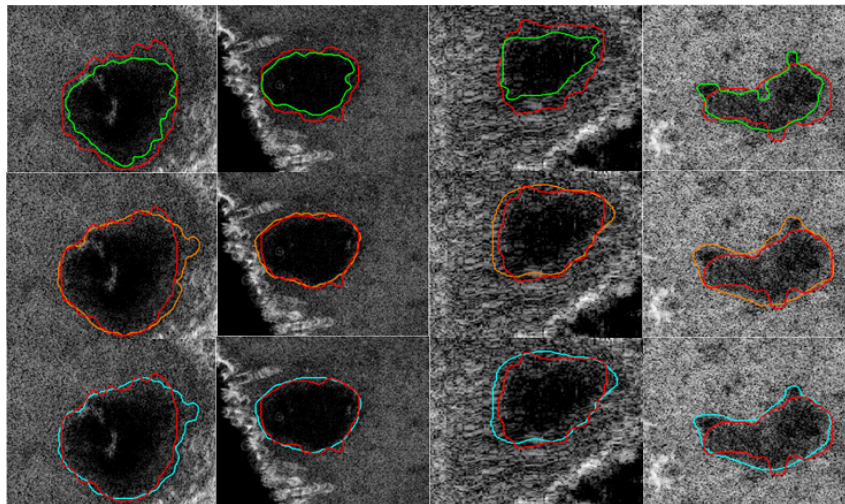
Figure 12. *Slices of segmentations. Top row: ADLL level set* [37]*. Middle row: LBM MRT D3Q7 lattice. Bottom row: LBM MRT D3Q19 lattice. First column: tumor Figure* 10(a)*. Second column: tumor Figure* 10(b)*. Third column: tumor Figure* 10(f)*. Last column: tumor Figure* 10(d)*. Reference contour in red.*

to obtain a fourth-order exact scheme without numerical diffusion. Moreover, the multigrid implementation allows obtaining relevant computation times for medical applications. Experiments have been conducted to validate the stability of the scheme. Comparisons with a BGK, SRT implementation have demonstrated the significance of the MRT approach. Finally, comparisons with the ADLL level set algorithm have proven that our solution is a good alternative to investigate the problem of underestimation of tumor volumes.

REFERENCES

[1] S. M. ALLEN AND J. W. CAHN, *A microscopic theory for antiphase boundary motion and its application to antiphase domain coarsening*, Acta Metallurgica, 27 (1979), pp. 1085–1095, https://doi.org/10.1016/0001-6160(79)90196-2.

[2] A. L. BERTOZZI, S. ESEDOGLU, AND A. GILLETTE, *Inpainting of binary images using the Cahn-Hilliard equation*, IEEE Trans. Image Process., 16 (2007), pp. 285–291, https://doi.org/10.1109/TIP.2006.887728.

[3] P. L. BHATNAGAR, E. P. GROSS, AND M. KROOK, *A model for collision processes in gases.* I. *Small amplitude processes in charged and neutral one-component systems*, Phys. Rev., 94 (1954), pp. 511–525, https://doi.org/10.1103/PhysRev.94.511.

[4] A. BRAIDES, *Gamma convergence for beginners*, Oxford Scholarship Online, (2007), https://doi.org/10.1093/acprof:oso/9780198507840.001.0001.

[5] T. M. BUI, A. CORON, L. BRIDAL, J. MAMOU, E. J. FELEPPA, E. SAEGUSA-BEECROFT, AND J. MACHI, *Random forest classification and local region-based, level-set segmentation for quantitative ultrasound of human lymph nodes*, 2015 IEEE International Ultrasonics Symposium (IUS), (2015), pp. 1–4, https://doi.org/10.1109/ULTSYM.2015.0106.

[6] F. CATTÉ, P. L. LIONS, J. M. MOREL, AND T. COLL, *Image selective smoothing and edge detection by nonlinear diffusion*, SIAM J. Numer. Anal., 29 (1992), pp. 182–193, https://doi.org/10.1137/0729012.

[7] B. CHEN, Y. LI, AND J. L. CAI, *Noisy image segmentation based on nonlinear diffusion equation model*, Appl. Math. Model., 36 (2012), pp. 1197–1208, https://doi.org/10.1016/j.apm.2011.07.073.

[8] H. Chen, S. Chen, and W. H. Matthaeus, *Recovery of the Navier-Stokes equations using a lattice gas Boltzmann method*, Phys. Rev. A, 45 (1992), pp. R5339–R5342, https://doi.org/10.1103/PhysRevA.45.R5339.

[9] J. Chen, Z. Chai, B. Shi, and W. Zhang, *Lattice Boltzmann method for filtering and contour detection of the natural images*, Comput. Math. Appl., 68 (2014), pp. 257–268, https://doi.org/10.1016/j.camwa.2014.05.023.

[10] J. W. Choi, H. G. Lee, D. Jeong, and J. Kim, *An unconditionally gradient stable numerical method for solving the Allen-Cahn equation*, Phys. A, 388 (2009), pp. 1791–1803, https://doi.org/10.1016/j.physa.2009.01.026.

[11] T. M. Cover and Y. A. Thomas, *Elements of Information Theory*, John Wiley & Sons, New York, 1991.

[12] F. Destrempes and G. Cloutier, *A critical review and uniformized representation of statistical distributions modeling the ultrasound echo envelope*, Ultrasound in Medicine and Biology, 36 (2010), pp. 1037–1051, https://doi.org/10.1016/j.ultrasmedbio.2010.04.001.

[13] D. D'Humieres, *Generalized lattice Boltzmann equations, 18th international symposium, rarefied gas dynamics, 1992 Vancouver, Canada*, Progress in Astronautics and Aeronautics, 159 (1992), pp. 450–458.

[14] D. D'Humieres, I. Ginzburg, M. Krafczyk, P. Lallemand, and L. S. Luo, *Multiple-relaxation-time lattice Boltzmann models in three dimensions*, Philos. Trans. A Math. Phys. Eng. Sci., 1792 (2002), pp. 437–451, https://doi.org/10.1098/rsta.2001.0955.

[15] L. R. Dice, *Measures of the amount of ecologic association between species*, Ecology, 26 (1945), pp. 297–302, https://doi.org/10.2307/1932409.

[16] F. Dubois and P. Lallemand, *Towards higher order lattice Boltzmann schemes*, J. Stat. Mech. Theory Exp., (2009), https://doi.org/10.1088/1742-5468/2009/06/P06006.

[17] C. M. Elliott, *The Cahn-Hilliard model for the kinetics of phase separation*, in Mathematical Models for Phase Change Problems, Internat. Ser. Numer. Math. 88, Birkhäuser, Basel, 1989, pp. 35–73, https://doi.org/10.1007/978-3-0348-9148-6_3.

[18] S. Esedoglu and Y.-H. R. Tsai, *Threshold dynamics for the piecewise constant Mumford-Shah functional*, J. Comput. Phys., 211 (2006), pp. 367–384, https://doi.org/10.1016/j.jcp.2005.05.027.

[19] I. Fonseca and L. Tartar, *The gradient theory of phase transitions for systems with two potential wells*, Proc. Roy. Soc. Edinburgh Sect. A, 111 (1989), pp. 89–102, https://doi.org/10.1017/S030821050002504X.

[20] M. E. Gurtin, *Generalized Ginzburg-Landau and Cahn-Hilliard equations based on a microforce balance*, Phys. D, 92 (1996), pp. 178–192, https://doi.org/10.1016/0167-2789(95)00173-5.

[21] W. Hundsdorfer and J. Verwer, *Numerical Solution of Time-Dependent Advection-Diffusion-Reaction Equations*, Springer Ser. Comput. Math. 33, Springer-Verlag, Berlin, 2003, https://doi.org/10.1007/978-3-662-09017-6.

[22] S. ichi Amari and S. C. Douglas, *Why natural gradient?*, in Proceedings of the IEEE International Conference on Acoustics, Speech, and Signal Processing (ICASSP), Seattle, WA, 4 (1998), pp. 1213–1216, https://doi.org/10.1109/ICASSP.1998.675489.

[23] B. Jawerth, P. Lin, and E. Sinzinger, *Lattice Boltzmann models for anisotropic diffusion of images*, J. Math. Imaging Vision, 11 (1999), pp. 231–237, https://doi.org/10.1023/A:1008304519705.

[24] J. Kim, J. W. Fisher, A. Yezzi, M. Cetin, and A. S. Willsky, *A nonparametric statistical method for image segmentation using information theory and curve evolution*, IEEE Trans. Image Process., 14 (2005), pp. 1486–1502, https://doi.org/10.1109/TIP.2005.854442.

[25] J. W. Kuo, J. Mamou, Y. Wang, E. Saegusa-Beecroft, J. Machi, and E. J. Feleppa, *Segmentation of 3-d high-frequency ultrasound images of human lymph nodes using graph cut with energy functional adapted to local intensity distribution*, IEEE Trans. Ultrasonics, Ferroelectrics, Frequency Control, 64 (2017), pp. 1514–1525, https://doi.org/10.1109/TUFFC.2017.2737948.

[26] P. Lallemand, *personal communication*, (2018).

[27] P. Lallemand and L.-S. Luo, *Theory of the lattice boltzmann method: Dispersion, dissipation, isotropy, galilean invariance, and stability*, Phys. Rev. E, 61 (2000), pp. 6546–6562.

[28] Y. Li and J. Kim, *Multiphase image segmentation using a phase-field model*, Comput. Math. Appl., 62 (2011), pp. 737–745, https://doi.org/10.1016/j.camwa.2011.05.054.

[29] Z. LI, M. YANG, AND Y. ZHANG, *Lattice Boltzmann method simulation of 3-d natural convection with double MRT model*, International Journal of Heat and Mass Transfer, 94 (2016), pp. 222–238, https://doi.org/10.1016/j.ijheatmasstransfer.2015.11.042.

[30] L. MODICA, *Gradient theory of phase transitions and the minimal interface criterion*, Arch. Ration. Mech. Anal., 98 (1987), pp. 123–142, https://doi.org/10.1007/BF00251230.

[31] P. NATHEN, D. GAUDLITZ, M. J. KRAUSE, AND N. A. ADAMS, *On the stability and accuracy of the BGK, MRT and RLB Boltzmann schemes for the simulation of turbulent flows*, Commun. Comput. Phys., 2 (2018), pp. 846–876.

[32] E. PARZEN, *On the estimation of a probability density function and mode*, Ann. Math. Stat., 33 (1962), pp. 1065–1076, https://doi.org/10.1214/aoms/1177704472.

[33] D. A. PERUMAL AND A. K. DASS, *A review on the development of lattice Boltzmann computation of macro fluid flows and heat transfer*, Alexandria Engineering Journal, 54 (2015), pp. 955–971, https://doi.org/10.1016/j.aej.2015.07.015.

[34] T. PHAM-GIA AND T. L. HUNG, *The mean and median absolute deviations*, Math. Comput. Modelling, 34 (2001), pp. 921–936, https://doi.org/10.1016/S0895-7177(01)00109-1.

[35] Y. QIAN, D. D'HUMIERES, AND P. LALLEMAND, *Lattice BGK models for Navier-Stokes equation*, Europhys. Lett., 17 (1992), pp. 479–484.

[36] B. SCIOLLA, P. CECCATO, L. COWELL, T. DAMBRY, B. GUIBERT, AND P. DELACHARTRE, *Segmentation of inhomogeneous skin tissues in high-frequency 3d ultrasound images, the advantage of non-parametric log-likelihood methods*, Phys. Procedia, 70 (2015), pp. 1177–1120, https://doi.org/10.1016/j.phpro.2015.08.253.

[37] B. SCIOLLA, L. COWELL, T. DAMBRY, B. GUIBERT, AND P. DELACHARTRE, *Segmentation of skin tumors in high-frequency 3-d ultrasound images*, Ultrasound in Medicine and Biology, 43 (2017), pp. 227–238, https://doi.org/10.1016/j.ultrasmedbio.2016.08.029.

[38] J. D. STERLING AND S. CHEN, *Stability analysis of lattice Boltzmann methods*, J. Comput. Phys., 123 (1996), pp. 196–206, https://doi.org/10.1006/jcph.1996.0016.

[39] Y. SUN AND C. BECKERMANN, *Sharp interface tracking using the phase field equation*, J. Comput. Phys., 220 (2007), pp. 626–653, https://doi.org/10.1016/j.jcp.2006.05.025.

[40] D. WANG, *Hybrid fitting energy-based fast level set model for image segmentation solving by algebraic multigrid and sparse field method*, IET Image Processing, 12 (2018), pp. 539–545, https://doi.org/10.1049/iet-ipr.2017.0786.

[41] G. W. WEI, *Generalized Perona-Malik equation for image restoration*, IEEE Signal Process. Lett., 6 (1999), pp. 165–167, https://doi.org/10.1109/97.769359.

[42] J. WEN, J. JIANG, AND Z. YAN, *A new lattice Boltzmann algorithm for assembling local statistical information with MR brain imaging segmentation applications*, Multidimens. Syst. Signal Process., 28 (2017), pp. 1611–1627, https://doi.org/10.1007/s11045-016-0436-x.

[43] D. A. WOLF-GLADROW, *Lattice-gas cellular automata and lattice Boltzmann models*, Lecture Notes Math. 1725, Springer-Verlag, Berlin, 2000, https://doi.org/10.1007/b72010.

[44] S. ZHAO, M. ZHOU, T. JIA, P. XU, Z. WU, Y. TIAN, Y. PENG, AND J. S. JIN, *Multi-branched cerebrovascular segmentation based on phase-field and likelihood model*, Computers and Graphics, 38 (2014), pp. 239–247, https://doi.org/10.1016/j.cag.2013.11.004.